Materials Today Chemistry 46 (2025) 102738

Contents lists available at ScienceDirect

Materials Today Chemistry

journal homepage: www.journals.elsevier.com/materials-today-chemistry/

From p to n type-semiconductor and metallic material: one-step route using femtosecond pulsed laser to produce Ag_3VO_4/ $AgVO_3$/Ag heterostructure

Guilherme Henrique Cruvinel [a], Rafael de Queiroz Garcia [b], Ivo Mateus Pinatti [c,*], Renan Augusto Pontes Ribeiro [d], Leonardo De Boni [b], Elson Longo [a,**]

[a] Functional Materials Development Center, Federal University of São Carlos, UFSCar, São Carlos, São Paulo, Brazil
[b] Photonics Group, Instituto de Física de São Carlos, Universidade de São Paulo, CP 369, 13560970, São Carlos, SP, Brazil
[c] Department of Chemistry, Federal University of Maranhão, Av. dos Portugueses, 1966, 65080-805, São Luís, MA, Brazil
[d] Department of Natural and Earth Sciences, State University of Minas Gerais, Av. Paraná, 3001, 35501-170, Divinópolis, MG, Brazil

ARTICLE INFO

Keywords:
Semiconductor
Ag_3VO_4
Femtosecond pulsed laser
$AgVO_3$
Plasmon effect
Heterostructure
DFT

ABSTRACT

The advent of femtosecond pulsed lasers has revolutionized materials science by enabling intense, ultrashort light pulses, facilitating nonlinear optical phenomena and structural modifications in materials. Ag_3VO_4, with its narrow band-gap, faces challenges such as charge recombination, leading to the exploration of doped and composite materials to improve efficiency in its applications. This work introduces a femtosecond laser irradiation method to produce intrinsic p-type (Ag_3VO_4)/n-type ($AgVO_3$) semiconductor heterostructures, along with metallic silver (Ag^0) with plasmon effect in one-step for the first time. The heterostructures were experimentally characterized (X-ray diffraction, Raman and Ultraviolet–visible spectroscopies, Field Emission Scanning Electron Microscope and Transmission Electron Microscopy) and discussed through quantum-mechanical, which provide insights into their structural, electronic, and vibrational properties and morphological analysis. X-ray diffraction and Raman spectroscopy indicated the presence of metallic Ag and β-$AgVO_3$, with plasmon effects, along with Ag_3VO_4. A detailed theoretical analysis revealed structural distortions and atomic environment influencing atomic charges, with β-$AgVO_3$ exhibiting more ionic Ag and V cations and significant O atom charge variations compared to Ag_3VO_4. Unexpected argentophilic and anion-anion interactions in β-$AgVO_3$ were identified, which may help in the understanding of silver nanoparticle growth under electron irradiation. The described production procedure provides the obtention of a new heterostructure, which may have the potential to its applications be explored.

1. Introduction

Since the 1960s, the advent of continuous-wave and pulsed lasers has provided access to high power coherent radiation, driving forward scientific and technological progress in materials science [1,2]. Among pulsed lasers, mode-locked femtosecond pulsed lasers produce intense ultrashort light pulses lasting around 10^{-15} s, around the duration of vibrational modes of molecules (from 10^{-14} to 10^{-12} s) [1,3–6]. Such pulses contain peak electric fields with amplitudes comparable to or much higher than the interatomic fields of materials. Hence, intense sources of radiation extrapolate the regime of linear optics, under which the light-matter interaction is independent of the light intensity, and a plethora of non-linear optical phenomena need to be considered [7,8]. In the realm of non-linear optics, high-power lasers can induce phenomena like second and third-harmonic generation, two-photon absorption, multiphoton, tunneling or avalanche/impact ionization, and stimulated Raman effects [7–10]. The low-order harmonic generation begins at intensities ranging from 10^9 to 10^{12} W/cm^2 [8]. Upon interacting resonantly with a target material, UV to IR femtosecond pulses drive electronic excitations, leading to carrier excitation, thermalization, removal, and various thermal and non-thermal effects [11,12]. Thermal conduction during femtosecond pulsed laser irradiation can be negligible, limiting thermally affected zones and microcracks after irradiation [4,8,13]. The incident pulses can excite electrons from transition to the conduction band, potentially weakening chemical bonds and enhancing atomic mobility without increasing lattice thermal

* Corresponding author.
** Corresponding author.
E-mail addresses: ivo.pinatti@ufma.br (I.M. Pinatti), elson.liec@gmail.com (E. Longo).

https://doi.org/10.1016/j.mtchem.2025.102738
Received 4 November 2024; Received in revised form 10 April 2025; Accepted 3 May 2025
Available online 12 May 2025

energy (non-thermal effect) [12,14–18]. This mechanism allows for structural alterations without necessitating thermal equilibrium [12, 16–18], as seen in theoretical calculations indicating a rise in local structural disorder within AgX (X: Cl, Br, and I) lattices under laser irradiation, where electronic temperature significantly influences electronic and structural changes [19].

The correlation between the composition, structure, and properties of materials has been widely published, including various synthesis and processing techniques that can result in distinct structural alterations, leading to corresponding changes in properties. Thus, manipulating synthesis and processing methods enables the attainment of desired property modifications [20]. Macedo et al. [21], Oliveira et al. [22], and Foggi et al. [23] works demonstrate the composition and processing of silver materials on bactericidal activity. According to their works, $AgVO_3$ exhibits greater potential for bactericidal activity compared to Ag_2MoO_4 and Ag_2WO_4 materials. Specifically, in the discussion of cube-shaped Ag_2WO_4, there is a notable change in the minimum bactericidal concentration upon electron and laser irradiation. The production of silver-based composites results in enhanced bactericidal activity, with laser irradiation leading to more substantial increases due to induced structural modifications favoring this activity. In contrast to traditional approaches, composite production by laser and electron irradiations involves the assembly of a new phase using atoms from the original structure, eliminating the necessity for organic or inorganic compounds in the process.

Silver orthovanadate p-type semiconductor (Ag_3VO_4) exhibits three polymorphs: α-phase, β-phase, and γ-phase [24–28]. These phases manifest the following distinct crystalline structures: monoclinic (α-phase), tetragonal (β-phase), and cubic (γ-phase) [24,26]. The interest in its photocatalytic activity stems from its narrow band-gap (1.95–2.58 eV) and efficient generation of charge carriers (free electrons and holes) that produce reactive oxygen species useful in pollutant decomposition [24,29–34]. However, issues such as photo-corrosion and rapid recombination of charge carriers hinder its performance, prompting research efforts to enhance its photocatalytic activity [32,35, 36]. Significant endeavors have been dedicated to enhancing the photocatalytic performance of materials, including incorporating doping techniques or utilizing composites/hybrids with low band-gap semiconductors to mitigate the recombination of photoinduced charge carriers [29,33,36,37]. Such endeavors, coupled with various other factors, have spurred the scientific community to explore numerous composite and hybrid materials, exemplified by NiO/Ag_3VO_4, Ag_3VO_4/ZnO, and Ag_3VO_4/C_3N_4/Reduced TiO_2 [37–39]. Furthermore, the literature reports that the phenomenon of surface plasmon resonance of silver particles on the surface can amplify visible light absorption, which may improve the photocatalytic activity response [40].

This work presents a different approach to producing $Ag_3VO_4/AgVO_3$/Ag heterostructure samples from Ag_3VO_4 using a one-step route: femtosecond pulsed laser irradiation. The heterostructure samples were experimentally characterized by field emission scanning electron microscopy (FE-SEM), transmission electron microscopy (TEM), UV–Vis diffuse reflectance and Raman spectroscopies, and X-ray diffraction (XRD). Also, *ab initio* quantum-mechanical calculations (DFT) were performed to provide an in-depth atomic-level comprehension to evaluate their structural, vibrational, electronic properties, chemical interactions, charges, and their distributions.

2. Experimental procedure

2.1. Synthesis

The procedure to synthesize silver orthovanadate (Ag_3VO_4) crystals for different synthesis times: 2^x (x: 1, 2, 3, 4, 5 and 6) min is based on *Cruvinel* et al. [41] work, which used microwaves-assisted hydrothermal method (MAHM).

To synthesize composite crystals a Ti:Sapphire laser was used, which emitted pulses with a temporal width of 150 fs (FWHM – full width at half maximum), with a central wavelength of 775 nm at a repetition rate of 1 kHz and energy per pulse of up to 400 μJ, with external neutral density filters to control the laser power. The laser beam was steered by mirrors and focused in the sample by a 200 mm focal length lens. The distance between the lens and the sample was finely controlled by a stepper motor, and the beam profile was chosen as large as possible for a certain desired irradiation intensity/fluence, reducing the irradiation time. The femtosecond pulsed laser irradiation system is represented schematicly in Fig. S1.

The sample was deposited on top of a quartz plate, which, in turn, was placed on a support that could carry out translational movements (two-dimensional stage) perpendicular to the incidence of the laser beam at a speed of 5 mm/s. The samples were irradiated along paths of parallel lines with a distance between two adjacent lines equivalent to the diameter of the laser beam on the sample, with values of fluences and laser peak intensities presented in Table S1. The irradiation routine was digitally controlled by a computer program developed in LabView.

The interaction between laser radiation and the samples caused instantaneous visual changes. The samples changed their colors from yellow-orange to grayish-black, which visually indicated the formation of the composite. The layer of Ag_3VO_4 deposited on the quartz plate was less than 2 mm; the incident laser did not completely penetrate the sample, part of the original sample was conserved. Then, a second round of irradiation for the same sample was performed, mixing it after the first irradiation. Finally, the irradiated powder was collected and stored in a microtube for further characterization. Fig. S2 shows the sample on the quartz slide during the irradiation process.

2.2. Characterizations

All samples were structurally characterized at long, medium, and short range (X-ray diffraction, Raman, and UV–Vis diffuse reflectance spectroscopies) and morphologically characterized by SEM and TEM. All samples were structurally characterized using Rigaku X-Ray Diffractometers, model D*Max*2500PC, Japan (Cu-Kα radiation; $\lambda = 1.5406$ Å; 2θ range: 10°–110°); model Ultima IV, Japan (Cu-Kα radiation, 2θ range: 10°–120°, scan speed: 0.0200°/second, tube voltage: 40 kV and tube current: 20 mA); and model SmartLab SE, Japan (Cu-Kα radiation, 2θ range: 15°–80°, scan speed: 0.5000°/minute, ω (incidence angle): 1°, mode: small incident angle, tube voltage: 40 kV and tube current: 50 mA). The diffraction patterns obtained for the composite samples were compared with ICSD (Inorganic Crystal Structure Data) crystallographic sheets No. 417469 [42], No. 82079 [43] e No. 181730 [44] referring to the Ag_3VO_4 (monoclinic structure), $AgVO_3$ (monoclinic structure) e Ag^0 (cubic structure) respectively. Morphological characterization was performed via scanning electron microscopy with a field emission gun (FEG-SEM), using a Carl Zeiss Supra 35-VP (Germany) operating at 5 kV, and transmission electron microscopy (TEM) using a FEI Tecnai F20, USA, (Accelerating Voltage: 200 keV, Beam Current: 1 nA) and FEI Tecnai G^2 F20 HRTEM (Accelerating Voltage: 200 keV, Beam Current: 1 nA), equipped with EDS (Energy Dispersive X-ray Spectroscopy) detector (Energy Resolution: 134 eV, Reference Energy: 5.9 keV, Minimum Energy: 100 eV, Detector Thickness: 3 mm, Detector Distance: 11.8 mm, Detector Angle: 14.6 deg, Detector Azimuth: 0 deg, Layer Definition: Edax from S/N 9577), microscopes. Raman spectroscopy (micro-Raman) measurements were conducted at room temperature, ranging from 50 to 1200 cm^{-1}, using a Micro-Raman iHR550 spectrometer (Horiba Jobin-Yvon, Japan) with a CCD detector and a He–Ne laser (Melles Griot, USA) operating at $\lambda = 633$ nm and a maximum power of 200 mW. Ultraviolet–visible diffuse reflectance spectroscopy (UV–Vis) measurements of irradiated silver orthovanadate powders were carried out at room temperature using a Varian Cary 5G spectrophotometer, USA (wavelength range: 400–800 nm).

2.3. Computational details

In this study, the structural, electronic, vibrational, topological properties, and charge distribution of the β-$AgVO_3$ semiconductor were examined by first-principles calculations at the density functional theory (DFT) level. The hybrid functional B3LYP [45,46] enhanced by Grimme-D3 dispersion interactions [47] as implemented in the CRYSTAL17 code [48] was used. Oxygen (O) and vanadium (V) centers were described by the all-electron 8-411d1 and 86-411d4G basis set, respectively, and the Hay-Wadt small core pseudopotentials (HAYWSC) 311d31G basis set was employed for silver (Ag) [49–51]. Electronic integration over the Brillouin Zone was carried out using a 6 × 6 × 6 Monkhorst-Pack k-point mesh [52]. The accuracy of the Coulomb and exchange integrals was controlled by a set of five tolerances (ITOL) set at 8, 8, 8, 8, and 14, determining the overlap criteria for when the overlap between two atomic orbitals is less than 10^{-ITOL} (10^{-8}, 10^{-8}, 10^{-8}, 10^{-8}, 10^{-14}). The self-consistent field (SCF) convergence criterion was set to 10^{-8} Hartree for the total energy difference between two subsequent cycles, while the four conditions for the geometry optimization, namely the root-mean-square (RMS) and the absolute value of the largest component of both the gradient and the estimated displacements, were set to 3.10^{-4}, $1.2.10^{-3}$, $4.5.10^{-4}$, and $1.8.10^{-3}$ atomic units, respectively. The.cif file used for β-$AgVO_3$ geometry optimization was ICSD crystallographic card No.: 82079 [43].

Harmonic approximation was used to calculate the vibrational frequencies at the Γ-point by diagonalizing the mass-weighted Hessian matrix [53–55]. The charge distribution, the value of the band gap, and the density of states (DOS) were used to complement the information on the electronic properties [48]. In particular, the charge distribution of the atoms in the structure was analyzed by combining a two-dimensional electron density difference map with different charge analysis methods (Mulliken, Hirshfeld, and Bader). To identify and evaluate the chemical interactions among the atoms within the structure, it was conducted a topological analysis of the electronic density

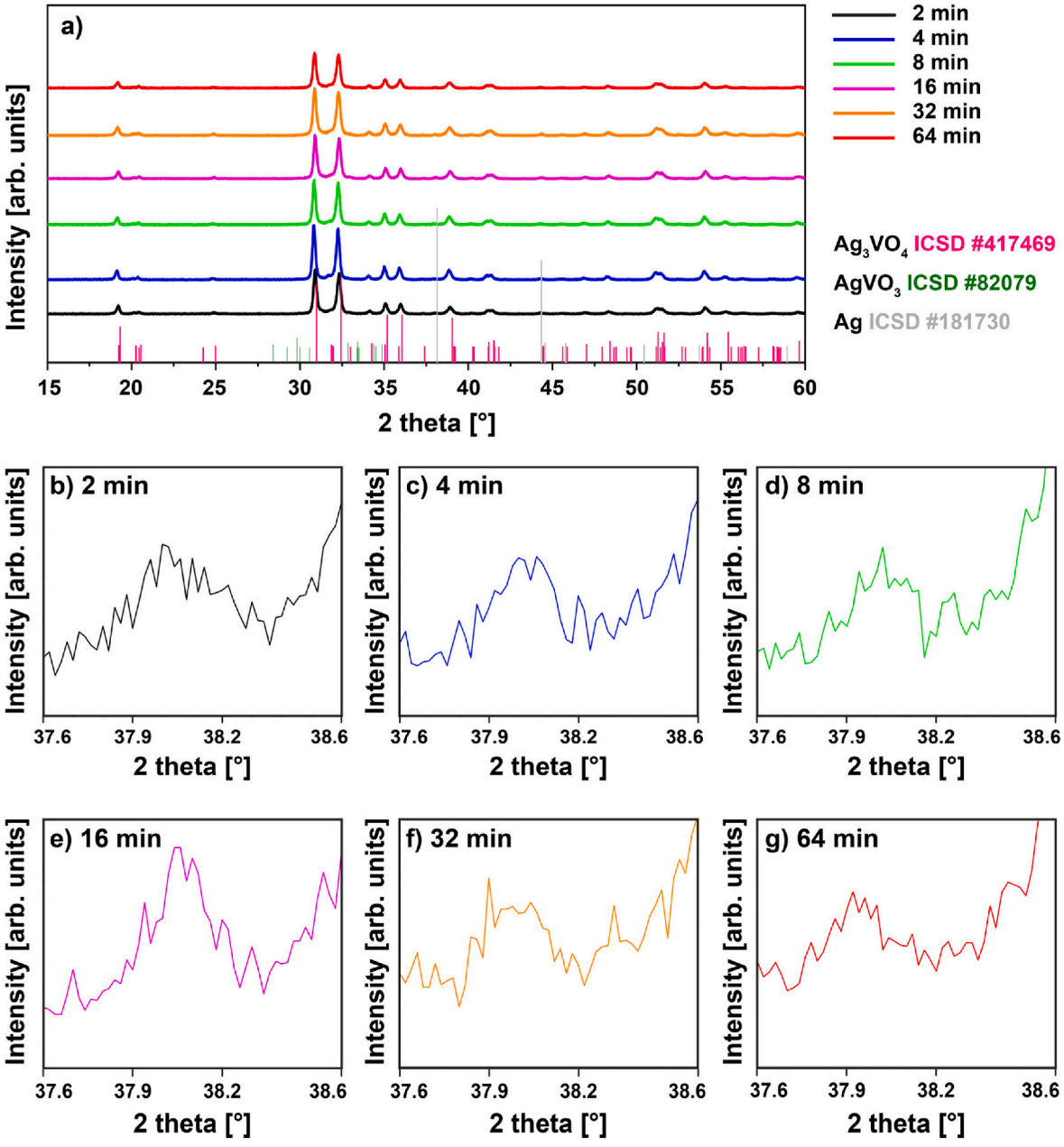

Fig. 1. XRD patterns of irradiated Ag_3VO_4 powders with the amplified region (in b) to g)) of the detected diffraction peak referring to metallic silver.

ρ(r) by using the TOPOND code [56]. This analysis focused on the study of the bond critical points, identified as (3, −1), which provide informations on the nature of the chemical bonds according to Bader's theory [57].

3. Results and discussion

3.1. Structural analysis

X-ray diffraction patterns of irradiated materials are shown in Fig. 1 and Fig. S3 to obtain information on the long-range structure.

All X-ray diffraction patterns of irradiated Ag_3VO_4 samples are following crystallographic cards No. 417469, No. 82079 and No. 181730 (Inorganic Crystal Structure Database - ICSD), which refers to monoclinic structure and *C2/c* spatial group (Ag_3VO_4) [26,27,42], monoclinic structure and *Cm* spatial group ($AgVO_3$) [43] and face-centered cubic structure and *Fm*-$\bar{3}$ *m* spatial group (Ag^0), respectively [44]. Low-intensity diffraction peaks for $AgVO_3$ and metallic Ag are observed, whose both of them may be associated to secondary phases [58] (minority). High structure long-range order is noticed, which it is indicated by the narrow and well-defined peaks for Ag_3VO_4 [58].

The $AgVO_3$ and metallic Ag materials are identified by a diffraction peak in 2θ between 29° and 30° (see Figures S3 a)-i) and b) and S4 a)), which are attributed to the Miller indices (401), (11 $\bar{1}$), (111), (310), (60 $\bar{1}$), (3 $\bar{1}$ 1), (602), according to crystallographic card No. 82079, and by a diffraction peak in 2θ between 37.6° and 38.4° (see Fig. 1 a) – g) and S3 a)-g)), which is attributed to the (111) Miller index, according to crystallographic card No. 181730, respectively. These X-ray diffractograms are important evidence to heterostructure formation.

Ag_3VO_4 synthesis showed slight long-range structural changes by employing the microwaves-assisted hydrothermal method and time synthesis as a manipulative synthesis parameter [41]. Moreover, X-ray diffractograms of irradiated samples do not show substantial changes in their long-range structure among the irradiated samples (see Fig. 1, S3, and S4 and Table S2). It was observed a slight left-shift of some peaks of the Ag_3VO_4 material in the irradiated samples compared to the irradiated 2-min sample. Compared to the original samples, main peak locations and their FWHM associated with Ag_3VO_4 materials in the irradiated samples do not represent significant alterations. Then, part of this change can be associated with the femtosecond pulsed laser irradiation that may provoke an increase in the interplanar distances of these planes, which means a small expansion in the volume of the unit cell for this observed left-shift [59,60] and, therefore, an increase in the long-range disorder.

According to *Miyasaka* et al. [61] study, it was evaluated ablation rate dependence on laser fluence (0.05–2.5 J/cm^2), incidence angle and polarization in irradiated copper, which resulted in ablation rate values superior to 1 nm/pulse on laser fluence values superior to 0.1 J/cm^2. Furthermore, thermal conduction during femtosecond pulsed laser irradiation may be neglected on samples, which means heat affected zone and microcracks are significantly reduced, and, consequently, the non-irradiated structure is just slightly affected [4,8,62–64]. As a result, slight changes in diffraction peaks observed in Ag_3VO_4 material and a small amount of metallic silver and $AgVO_3$ presented on X-ray diffractograms may be justified on samples, whose irradiation laser effects may have occurred substantially in the regions where there were phase decomposition.

Ab initio calculations were performed for $AgVO_3$ to confirm its presence in the sample and also to characterize the changes caused by it. Quantum mechanics calculations already reported by the literature were performed for Ag_3VO_4 [41].

The local coordination analysis provides four types of clusters for the monoclinic structure of β-$AgVO_3$ composed of Ag, V, and O atoms: four [VO_6] clusters and four [AgO_x] (x = 5, 6 and 7) clusters, whose vanadium atoms are coordinated by six oxygen atoms and silver atoms are coordinated by five (2x), six and seven oxygen atoms. According to *Oliveira* et al. [65] and *Beltrán* et al. [66], [AgO_x] clusters have two distorted square pyramids (x = 5/Ag_5–$_1$O and Ag_5–$_2$O), distorted octahedra (x = 6) and distorted deltahedra (x = 7) coordination. *Rozier* et al. [43] work considers that V–O chemical bonds build zigzag chains of edge-shared [VO_6] octahedra. Theoretical results of this work confirmed these structures (see Fig. 2 and S5).

Table S3 shows lattice parameters and the X–O chemical bond distance (X: Ag or V) in the $AgVO_3$ structure obtained by this work and literature [43,65], which shows a good agreement. Similar to Ag_3VO_4 structure reported in the literature [41], $AgVO_3$ has longer V–O chemical bond distances than Ag–O chemical bond distances, as expected, and its chemical bond distances vary intra and interclusters for the same central chemical element. Moreover, $AgVO_3$ results show a larger volume (≈8.8 %) and diversity of clusters in its structure compared to Ag_3VO_4 structure (V: 463.474 Å^3) [41]. Properties may change by distortions observed in chemical bonds proportionated by different synthesis methods and materials, which can enable different applications for materials [65].

Fig. 3 presents the normalized Raman spectra for the irradiated Ag_3VO_4 samples and Tables S4 and S5 display both the theoretical and/or experimental wavenumbers for each active Raman vibrational mode for Ag_3VO_4, composite, α-$AgVO_3$, and β-$AgVO_3$.

The α-phase silver orthovanadate exhibits 21 theoretical active Raman modes [41]. Ag_3VO_4 Raman spectra synthesized by MAHM presented 10 broad active Raman modes, and time synthesis chosen was not enough to produce significant changes in the short-range structure. Raman peaks were assigned according to theoretical results obtained by *Cruvinel* et al. [41].

Fig. 3 shows that all the spectra exhibit 14 Raman-active modes. Alterations observed in the Ag_3VO_4 spectra profiles compared to the irradiated ones are consistent across all samples [41].

The ultrashort pulsed laser irradiation offers two effects on the target material: thermal and non-thermal [12]. The temperature reached by the lattice may be enough to induce phase transitions and ablation of materials through thermal effects [12]. Photoexcitation may transfer electrons sufficiently from bonding (valence band) to antibonding (conduction band) states, causing the lattice to weaken (approximately 10 % of electrons from valence band to conduction band), and become non-thermally disordered, due to modifications of interatomic forces [12,14,15,67]. To illustrate these effects, the literature reports three regimes of excitation for GaAs semiconductors [12,14,68–71]: in low fluence (below 0.5 kJ m^{-2} or 50 % of the threshold for irreversible structural change of 1.0 kJ m^{-2}), rapid Auger recombination and phonon emission occur, inducing lattice heating; in intermediate fluence (0.5 kJ m^{-2}/50 % - 0.8 kJ m^{-2}/80 % of threshold fluence), electronic

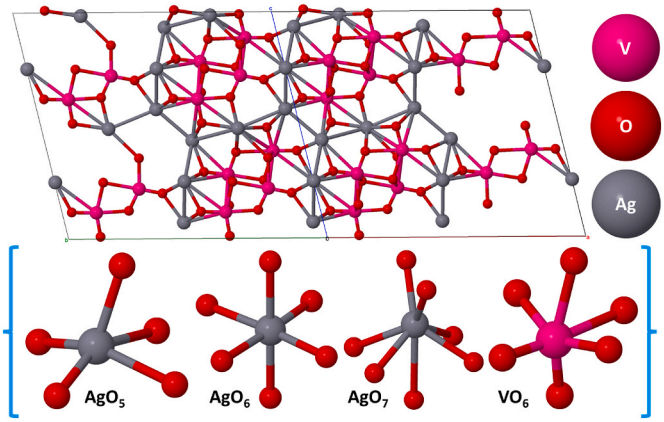

Fig. 2. – Schematic representation of optimized monoclinic crystalline structure of $AgVO_3$ and its coordination polyhedra. Vanadium, oxygen and silver atoms are represented by pink, red and gray colors, respectively.

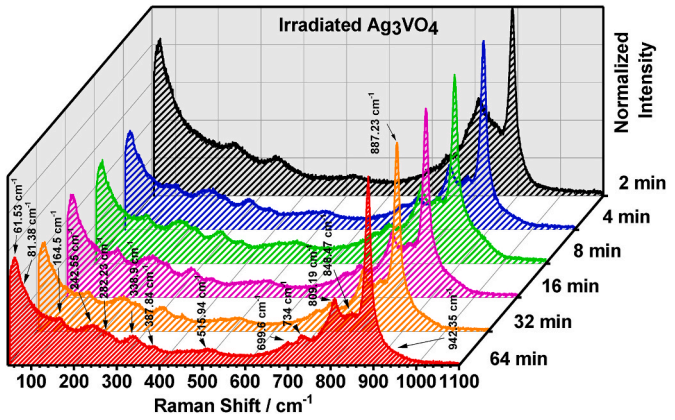

Fig. 3. – Experimental Raman spectra for irradiated Ag_3VO_4 obtained by FPL.

effects are stronger, and the dielectric function indicates a non-thermal long-range order-disorder transition; a non-thermal semiconductor-to-metal transition is observed above 80 % of threshold fluence.

Concerning temperature effects on Ag_3VO_4, Vali et al. [24] found that electrodeposited silver orthovanadate films were completely decomposed at 300 °C, leading to the formation of $Ag_4V_2O_7$, oxygen, and metallic silver, whose experimental data was supported by thermodynamics calculation, which showed it is the lowest Gibbs free energy pathway ($\Delta G^{\circ} = +0.609$ eV). Cloet et al. [26] reported Ag_3VO_4 thin films prepared by combinatorial sputtering and continuously heated up to 450 °C. From 225 °C to 390 °C, it was observed metallic Ag and β-$AgVO_3$ formation in high-temperature X-ray diffraction. This result shows this endothermic reaction found another reaction pathway, whose Gibbs free energy is slightly greater ($\Delta G^{\circ} = +0.643$ eV [24]) than that reported by Vali et al. [24] for the lowest Gibbs free energy pathway among the considered reactions. X-ray diffraction peaks indicate $AgVO_3$ and metal Ag formation by FPL, which correspond to the same reaction pathway followed by the result presented by Cloet et al. [26]. Furthermore, it is noted important modifications (relative intensities, peak shifts, number of experimental Raman-active modes, spectra profile) in the composite Raman spectra compared to original samples (Ag_3VO_4). The behavior of composite Raman spectra is very similar to those reported by *Oliveira* et al. [65] for β-$AgVO_3$. For this reason, theoretical simulations were performed for $AgVO_3$, and experimental data provided by literature may help to verify it.

Fig. S6 presents the Raman spectra of the composite. More details as theoretical and/or experimental Raman-active modes obtained in this work and literature for composite, α-$AgVO_3$ [22,72], β-$AgVO_3$ [65, 72–76], and Ag_3VO_4 [41] and their vibration types (this work and literature [72–75,77]) are provided in Tables S4, S5 and S6.

Fig. 3 and S6 show the normalized Raman spectra for the irradiated Ag_3VO_4 samples. Theoretical peaks (β-$AgVO_3$), corresponding to experimental peaks, are observed at 59.08, 87.57, 168.37, 245.03, 280.67, 333.45, 374.94, 511.44, 718.82, 746.71, 815.37, 844.18, 885.12 and 938.09 cm^{-1}. The peaks are due to various types of vibrations - twisting, wagging, rocking, bending, and stretching - involving V–O and Ag–O bonds of [VO_6] and [AgO_x] clusters. The vibration frequencies entail complex and coordinated atomic vibrations within this material. Beyond the frequency of 374.94 cm^{-1}, a decrease in the active contribution of Ag atoms to atomic vibration is observed. Fig. S6 and Table S4 demonstrate a close alignment between theoretical and experimental data.

Analysing Tables S4 and S5 and Fig. S6, peaks at 300 cm^{-1}, 400 cm^{-1}, 700 cm^{-1}, 750 cm^{-1} and 950 cm^{-1} are not observed in the literature [41] for Ag_3VO_4 semiconductor. Furthermore, considering *Oliveira* et al. [65] work, whose Raman-active modes number for α-$AgVO_3$ material is larger and presents a better correspondent position compared to composite Raman peaks, it is noted a peak in about 250 cm^{-1}, 400 cm^{-1}, and 700 cm^{-1}, which are not observed in composite Raman spectrum. Although Raman peaks lower than 100 cm^{-1} for β-$AgVO_3$ are not observed in this literature, these peaks are predicted by theoretical calculations. Based on these comparisons, X-ray diffraction results in this work, and Raman spectra profile observed in *Oliveira* et al. [65] work, composite Raman spectra may correspond to β-$AgVO_3$ Raman spectra.

Electromagnetic enhancement by the plasmon effect occurs when colloidal metal particles (substrate), smaller than the laser wavelength, interact with an oscillating electromagnetic field, causing oscillation of electrons on the surface particle, which may generate an electromagnetic field in addition to the incident electromagnetic radiation, resulting in an increased signal of the nearby adsorbed analyte [78,79]. It allows the detection of trace contaminants and nearly imperceptible Raman peaks [79,80], with silver being the most effective metal as substrate [80]. It provides remarkable sensitivity and selectivity, allowing for the detection of analytes in complex mixtures without separation [79]. Theoretical models show that the closer an analyte molecule is to the metal particle, the greater the enhancement [78]. The electromagnetic field strength decreases with the third power of the distance from the metal particle (spherical model), meaning maximal enhancement occurs when the analyte is in direct contact with the metal surface [78]. This theory is most effective when metal particles are small relative to the laser wavelength (typically radius of the particle is less than one-tenth of the wavelength) [78].

The femtosecond pulsed laser contains a very high peak flux of photons [81]. When these photons interact with matter, they significantly increase the electron density in the conduction band by exciting electrons from the valence band and structural defects [81,82]. This process can cause permanent distortions in atomic positions, leading to changes in the angles and length of chemical bonds, amorphization of the irradiated region, and a significant increase in the formation of silver vacancies [19,81–84], which may contribute to broadening the Raman spectra - under identical experimental characterization conditions - [83, 85–90]. Unlike previous studies involving n-type semiconductors [81, 82], the laser treatment may have increased the p-type character of the Ag_3VO_4 p-type semiconductor. However, literature indicates this material is sensitive to low to moderate temperatures, showing signs of chemical decomposition around 225 °C [26]. From the above-mentioned observations and according to our interpretation, laser irradiation can induce structural disorders such as amorphization and Ag vacancy formation, enhancing the p-character of this semiconductor, which may be observed partially for diffractogram peaks associated with Ag_3VO_4 material in the irradiated samples. Additionally, the resulting temperature increase and/or non-thermal effects are likely to induce structural instability, leading mainly to the decomposition of the sample in the irradiated region and producing $AgVO_3$ (n-type semiconductor) along with some metallic silver. Part of metallic silver may also arise from $AgVO_3$ semiconductors, as observed in works using electron beam irradiation and other silver-based semiconductors [65,81,82]. The nearby formed metallic silver to β-$AgVO_3$ semiconductor on those samples may present similar conditions to that one related to the plasmon effect, which would explain Raman spectra of the irradiated samples similar to the β-$AgVO_3$ Raman spectra. The plasmon effect from the silver particles probably enhances the Raman signal from the $AgVO_3$ structure, significantly altering the Raman spectrum profile compared to the non-irradiated Ag_3VO_4 samples. Based on our interpretation, a lower defect density in $AgVO_3$ plays a crucial role in shaping the Raman spectrum, which accounts for the observed peak narrowing in the irradiated samples.

3.2. Surface and morphological analyses

Figs. 4 and 5 exhibit FE-SEM and TEM images of irradiated Ag_3VO_4 particles respectively. All samples display predominantly irregular

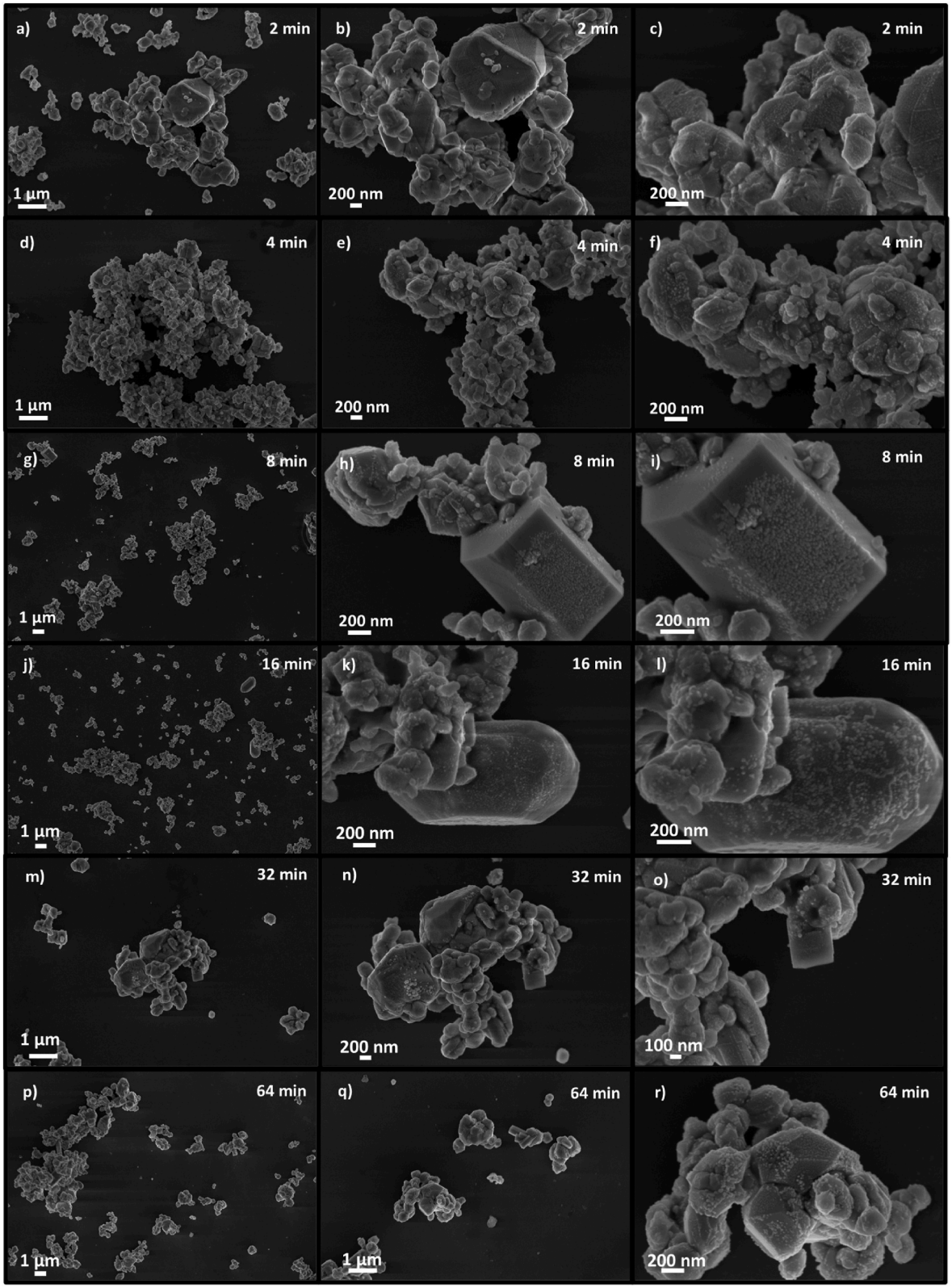

Fig. 4. – FE-SEM images in different magnifications of irradiated Ag_3VO_4 synthesized by MAHM: a), b) and c) at 2 min; d), e) and f) at 4 min; g), h) and i) at 8 min; j), k) and l) at 16 min; m), n) and o) at 32 min; p), q) and r) at 64 min.

morphologies, with some regions demonstrating regular shapes, and a significant degree of agglomeration/aggregation. Furthermore, a broad size distribution is observed, ranging from tens of nanometers to 1 µm in detectable particle size. These morphological characteristics are observed in Ag_3VO_4 samples synthesized by MAHM [41]. Also, distinct morphologies can be associated with the heterostructure formed by different silver phases (Ag_3VO_4, $AgVO_3$ and metallic Ag), as discussed in the XRD section.

Moreover, the interaction between the electron beam produced by a scanning electron microscope and a silver-based semiconductor can

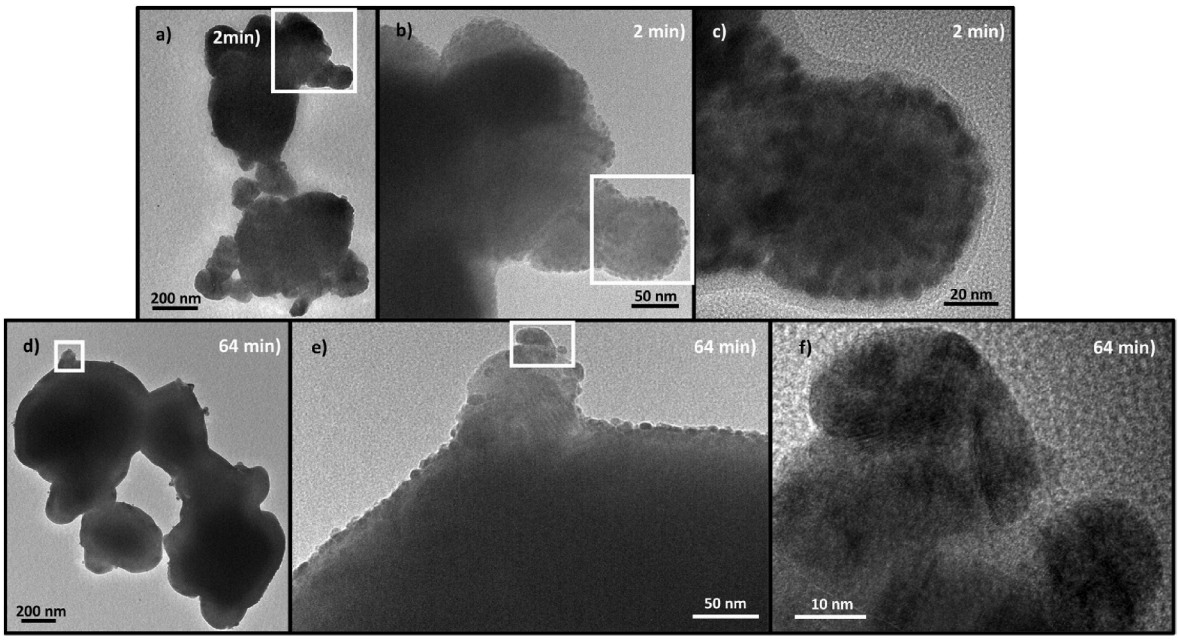

Fig. 5. – Transmission electron microscopy images of irradiated Ag_3VO_4 synthesized by FPL: a), b) and c) synthesized in 2 min by MAHM and d), e) and f) synthesized in 64 min by MAHM in different magnifications.

provide *in situ* metallic silver nucleation and growth on the surface, which may be observed in Fig. 4 – h), i), k) and l). This effect was observed and discussed for Ag_3VO_4 and $AgVO_3$ in *Cruvinel* et al. [41] and *Oliveira* et al. [65] studies respectively.

Figure S7 displays the EDS spectra for irradiated samples synthesized by MAHM at 64 min. Oxygen (O), silver (Ag), and vanadium (V) elements were detected, aligning with the expected composition of the sample (Ag_3VO_4, $AgVO_3$, and Ag^0). Notably, there is no evidence of impurities. The composition was tabulated in Fig. S7, however our analysis is limited to a qualitative approach (i.e., element identification) [91,92].

3.3. Optical and electronic analysis

UV–Vis diffuse reflectance spectra of the irradiated samples are presented in Fig. S8. Spectra provided absorption in the visible range of about 570 nm and the presence of the Urbach tail [93], which is identified by a non-linear decrease in reflectance. According to the literature, silver orthovanadate is a p-type semiconductor [24,28] and silver metavanadate is an n-type semiconductor [65]. As semiconductors, these materials have intrinsic defects and other structural changes produced by experimental methodologies that may provide changes in their local density of states, which may also contribute to Urbach tail formation.

Interaction between femtosecond pulsed laser and silver-based materials may cause segregation, nucleation, and growth processes of metallic silver in the samples [21], as observed in this work. At the nanometric scale, metallic materials may present a surface plasmon resonance phenomenon. It is well-known in the literature that silver nanoparticles cause absorption of visible-range electromagnetic radiation due to this phenomenon, and absorption band intensity is susceptible to silver nanoparticle concentration [89,94,95]. According to *AZIZ* et al. [94], it was detected silver nanoparticles absorbed at a wavelength of about 420 nm. *TAN* et al. [95] reported that increasing the silver nanoobjects size caused absorption peak shift to longer wavelengths, from 546 nm to 1130 nm for particle sizes of about 30 nm and 210 nm, respectively. So, it is reasonable to assert absorption region of silver nanoobjects may coincide with the absorption region of Ag_3VO_4 (see Fig. S8), which should change the stimated band-gap values and spectra obtained.

X-ray diffraction showed β-$AgVO_3$ is one of the constituents of the irradiated samples. Literature reports its band gap may range from 1.88 eV to 2.04 eV [65], corresponding to photon absorptions with wavelengths of approximately 659 nm–607 nm respectively. Its absorption band is similar to the silver orthovanadate absorption region, which is influenced by the degree of order-disorder at the electronic structure. Intermediary energy levels may be created within the crystal band gap due to the defects in the structure (incorporating donor and/or acceptor dopants or vacancies) [96–104]. Ag nanoparticles formation may generate defects in the Ag_3VO_4 and $AgVO_3$ structures due to stoichiometric changes, and as a consequence, may contribute to its electronic level variations [41,65,81]. So, it is reasonable to assert the absorption region of silver nanoobjects and $AgVO_3$ may coincide with the Ag_3VO_4 absorption region [41], which should change the band-gap values and spectra obtained. Therefore, both materials may contribute to obtained spectra and make it inadequate to obtain the stimated values related to the optical band-gap for a single material.

According to DFT simulations for $AgVO_3$ (see Fig. 6 a), electron levels from Ag and O atoms are the main ones responsible for contributing to the formation of the upper part of valence band (VB), while electron levels from V atoms constitute the lower region of conduction band (CB). Furthermore, theoretical calculations suggest a Z' (300) *k*-point direct electronic transition and a band-gap energy of 2.48 eV. *MENEZES* et al. [105] carried out the synthesis for β-$AgVO_3$ by different chemical routes and obtained band-gap energy values corresponding to 1.72 eV, 1.90 eV, 2.45 eV, and 2.50 eV. Therefore, these findings align with the results documented in the literature.

Fig. 6 b) and c) show the band structure and the projected density of states on silver atoms, considering all silver atoms in a unit cell (4 atoms) and only single non-equivalent silver atoms (AgO_5, AgO_6, and AgO_7: 4 atoms), respectively. They reveal that the constribution to the bands of each Ag is different since it depends significantly on the type of coordination and on the chemical environment. Indeed, the AgO_5 and AgO_6 are dominant closer the Fermi level, while the AgO_7 contributes to an inner VB region. Additionally, in the AgO_5 clusters (same coordination number) are observed different electron level shifts and intensities in the uppermost VB, being $AgO_{5\text{-}1}$ the dominant closer the Fermi level. The literature reports the contribution to the intensity in the density of states near the VB maximum shows no substantial difference for Ag_3VO_4 [41].

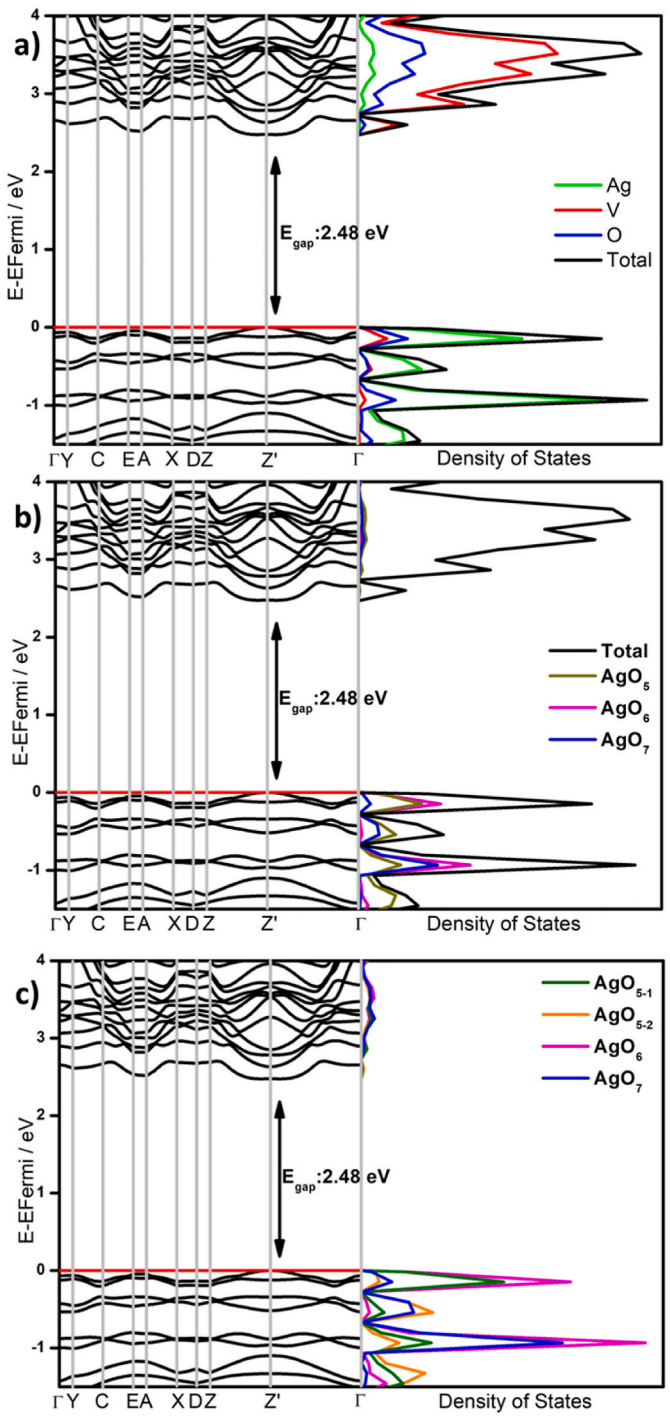

Fig. 6. – Band structure and density of states projected in a) all atoms (20 atoms per cell); b) all silver atoms in their different clusters (AgO_x; x: 5, 6 and 7) (4 atoms per cell); c) all non-equivalent silver atoms (AgO_5: 2, AgO_6: 1 and AgO_7: 1 atom per cell) for $AgVO_3$.

Therefore, distortions in chemical bondings may or not make significant changes in electronic structure.

Cruvinel et al. [41] work reports electron charge distribution, 2D charge density difference map, and charge density topological analysis for Ag_3VO_4. Based on that, a similar study was performed for the $AgVO_3$ structure in this work to evaluate chemical interactions and charge distribution changes in this structure, which is produced after laser irradiation.

Atomic charges for the different species in the $AgVO_3$ are shown in Table S7. A slight difference between Mulliken charges and Hirshfeld and Bader charges is observed. Bader charges results agree with those values previously reported by *Oliveira* et al. [65] for V and Ag atoms. According to Table S7 (in absolute values), for silver atoms: Mulliken charges vary from +0.701 to + 0.745, Hirshfeld charges vary from +0.734 to + 0.780, Bader charges vary from +0.765 to + 0.788; for vanadium atoms: Mulliken charges vary from +2.057 to + 2.076, Hirshfeld charges vary from +2.245 to + 2.269, Bader charges vary from +2.270 to + 2.290; for oxygen atoms: Mulliken charges vary from - 1.161 to - 0.783, Hirshfeld charges vary from - 1.256 to - 0.885, Bader charges vary from - 1.173 to - 0.926. Oxygen atoms show the largest range for atomic charges in $AgVO_3$ structure.

The original structure (Ag_3VO_4) may be severely altered when removing atoms by laser irradiation to produce other phases (metallic Ag and $AgVO_3$) in the system. These results indicate a partially ionic nature of the chemical bonds present in this structure as for Ag_3VO_4 [41]. In this new atomic rearrangement ($AgVO_3$), O atoms have the most affected atomic charges – see Table S6 and Fig. 7. Furthermore, compared to the Ag_3VO_4 structure, Fig. 7 a) and b) show a larger atomic charge for Ag and V atoms in the $AgVO_3$ structure, independently of the approach chosen, which reveals these atoms become slightly more ionic. For O atoms, Fig. 7 c), the atomic charges indicate some oxygen atoms become more anionic and other ones less anionic for $AgVO_3$.

Although silver atoms have different coordination numbers (AgO_5, AgO_6, and AgO_7) and different distortions (e.g. $AgO_{5\text{-}1}$ and $AgO_{5\text{-}2}$) of chemical bonding, the atomic charges present in these silver atoms and in vanadium atoms are not significantly affected in $AgVO_3$. Our interpretation of a larger range of atomic charges for the oxygen atoms is explained by the different neighboring atoms and different numbers of each chemical element (V, Ag, O) that the structure can provide to make a chemical interaction with the oxygen atom, which change the way the charge is distributed on these atoms.

As for Ag_3VO_4 structure [41], the 2D difference electron density map (Fig. 8) for $AgVO_3$ indicates charge transfers from vanadium and silver atoms (in blue) – oxidative process - to oxygen atoms (in red) – reduction process, which indicates the formation of cations and anions respectively in $AgVO_3$ structure, as expected. Such results are according to atomic charge results shown in Table S7.

As shown in X-ray diffraction anallysis, silver atoms are coordinated by oxygen atoms producing three coordination polyhedra in $AgVO_3$ structure: the first one is the distorted square pyramid (AgO_5), whose local structures have different distortions producing $Ag_{5-1}O$ and $Ag_{5-2}O$ structures. Table S8 presents 6 chemical bonds associated with these two local structures, which have repeated and different chemical bond lengths; the second one is the distorted octahedral structure (AgO_6), whose local structure has six chemical bonds, four of them with different chemical bond lengths and two are equivalent chemical bondings lengths; the last one is the distorted deltahedra (AgO_7), which have seven chemical bonds in this local structure, but considering there are equivalent chemical bonds, Table S8 present four different ones. Table S8 provides chemical interactions between different silver atoms of distinct square pyramid coordination polyhedra ($Ag_{5-1}O$ and $Ag_{5-2}O$) and three chemical interactions among oxygen atoms in this structure. Argentophilic interaction is theoretically identified also in Ag_3VO_4 [41].

The octahedral coordination polyhedra consists of vanadium atoms coordinated with six oxygen atoms, resulting in six chemical bonds, five of which exhibit distinct chemical bong lengths. Distortion in the local structure yields four octahedral formations, consequently generating twenty non-repeating critical points for these chemical bonds. Additional unexpected anion-anion chemical interactions (O–O) are observed in this structure.

The majority of discerned chemical interactions are categorized as transit in $AgVO_3$ according to the procedure described by literature [106–108], indicating a partially covalent interaction. In particular, topological analysis shows four of V–O chemical interactions involved in (VO_6) polyhedral are classified as transit, which is analyzed in terms of

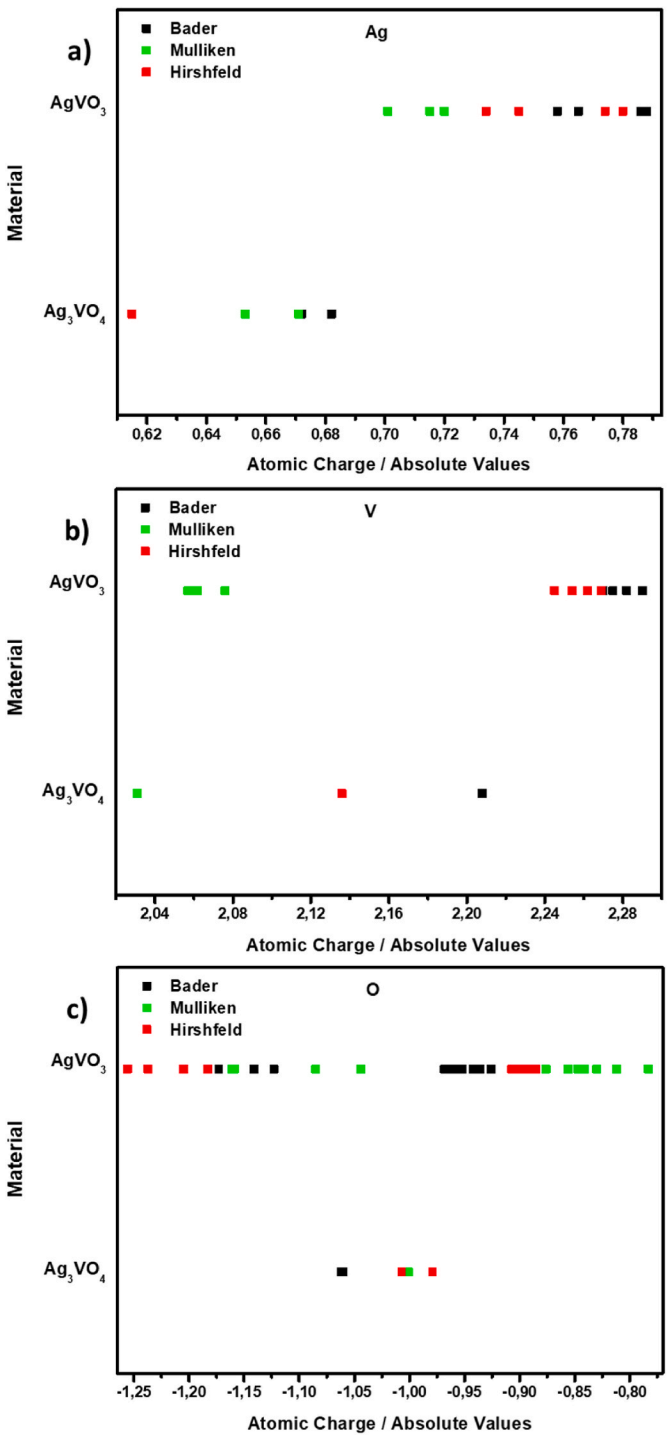

Fig. 7. – Computed atomic charges for all different Ag (in a), V (in b)) and O (in c)) atoms present in the structure of the Ag_3VO_4 [41] and $AgVO_3$ using Mulliken, Hirshfeld and Bader theories.

$\nabla^2\rho > 0$ and $H < 0$ [106,107]. Additionally, H/ρ ratio <0 indicates covalence degree (CD) [106] and the highest values found for $|H|/\rho$ ratio (bond degree) (0.156–0.504 a.u.), and for $|V|/G$ ratio (1.120–1.328) means the strongest and most covalent in nature for these chemical interactions [106,109] in $AgVO_3$ structure. Their electron densities (0.116–0.221 e/Å^3) are similar to partial covalence for strong H–O hydrogen bonds ($0.05 < \rho < 0.12$ a.u) in molecular crystals and covalent interactions $\rho > 0.14$ a.u. [108]. The longest V–O chemical interactions in each (VO_6) polyhedral have electron density, $|V|/G$ ratio, and $|H|/\rho$ ratio ranging from 0.021 to 0.062 e/Å^3, from 0.955 to 1.000 and from 0.000 to 0.051 a.u. in their critical points respectively, which may be classified as closed shell ($\nabla^2\rho > 0$ and $H > 0$). Such chemical interactions are related to ionic or weak intermolecular interactions. As mentioned before, *Rozier* et al. [110] reported [VO_6] octahedra as part of the $AgVO_3$ structure, which is identified in this work by these six critical points among V–O chemical bonds. However, the topological analysis shows that structural distortions are sufficient to cause significant changes in the classification of the chemical nature of two of the chemical bonds present in this coordination sphere.

Ag–O chemical interactions may be classified as transit ($\nabla^2\rho > 0$ and $H < 0$), and H/ρ ratio indicates covalence degree (CD), there are different chemical characteristics for these interactions. The lower values found to $|V|/G$ ratio (0.992–1.123) and $|H|/\rho$ ratio (0.009–0.150 a.u.) indicate weaker and more ionic chemical interaction compared to V–O interactions, and their lower electron density (0.014–0.058 e/Å^3) correspond to electron densities in ionic crystals (lower than 0.04 a.u.) [111]. Similar to V–O interactions, some Ag–O interactions present more ionic character than others in this structure. Table S8 also provides two Ag–O interactions ($AgO_{5\text{-}2}$ and AgO_7), which may be classified as closed shells ($\nabla^2\rho > 0$, $H > 0$, and low electron density). Such as chemical interactions may be related to ionic interactions, and $|H|/\rho$ ratio >0 indicates softening degree (SD) [106,107], whose this AgO_7 interaction represents a weaker and greater closed shell interaction in nature (greater SD magnitude [106,109]).

Regarding unexpected chemical interactions: Ag–Ag chemical interaction (argentophilic interaction) has electron density equivalent to 0.009 e/Å^3, $|V|/G$ ratio equal to 0.905, and $|H|/\rho$ ratio equivalent to 0.069 a.u. in its critical point, which may be classified as closed shell ($\nabla^2\rho > 0$ and $H > 0$) [106–108]. Such chemical interactions are related to ionic or weak intermolecular interactions [108,112]; O–O chemical interactions have electron density, $|V|/G$ ratio, and $|H|/\rho$ ratio ranging from 0.023 to 0.038 e/Å^3, from 0.967 to 1.024, and from 0.020 to 0.030 a.u. in their critical points respectively. However, two of these chemical interactions are classified as transit ($\nabla^2\rho > 0$ and $H < 0$), which makes them similar to Ag–O interactions, and another one as closed shell (intermolecular interactions) ($\nabla^2\rho > 0$ and $H > 0$). O–O transit and closed-shell interactions have already been identified in polymorphs of SiO_2 earlier [113,114]. More details about anion-anion interactions in crystals may be found in *Nelyubina* et al. [115], and about cation-cation and anion-anion interactions in *Korabel'nikov and Zhuravlev* [109] study.

It is interesting to note there are anion-anion and cation-cation chemical interactions in the $AgVO_3$ structure. The literature reports several examples of this kind of interactions in metal-organic nitrate, $KClO_4$, $NaClO_4$, $LiClO_4$, $LiNO_3$, and other crystals [109]. These interactions play a fundamental role in the stabilization of material structures, which was discussed in detail by *Nelyubina* et al. study [115].

Based on these findings, it is possible to argue that laser irradiation stimulation induces a higher number of defects on Ag_3VO_4 generating β-$AgVO_3$ and metallic Ag particles. Indeed, Ag_3VO_4 crystalline structure exhibits a more regular distribution, containing distorted seesaw and distorted square planar AgO_4 clusters, that becomes more disordered in β-$AgVO_3$ associated with step-by-step defect mechanisms that connects both chemical compositions. As a consequence, the existence of structural defects contributed to the electronic structure transition from p-type (Ag_3VO_4) to n-type ($AgVO_3$) semiconductor behavior, and, finally the existence of metallic features associated with the clusterization of silver atoms on the surface of the obtained morphologies.

4. Conclusions

This study reports for the first-time the production of heterostructures consisting of Ag_3VO_4 (p-type semiconductor), β-$AgVO_3$ (n-type semiconductor), and metallic Ag with plasmon effect using femtosecond pulsed laser irradiation on single-phase Ag_3VO_4 samples. X-ray diffraction confirmed the presence of silver phases in the

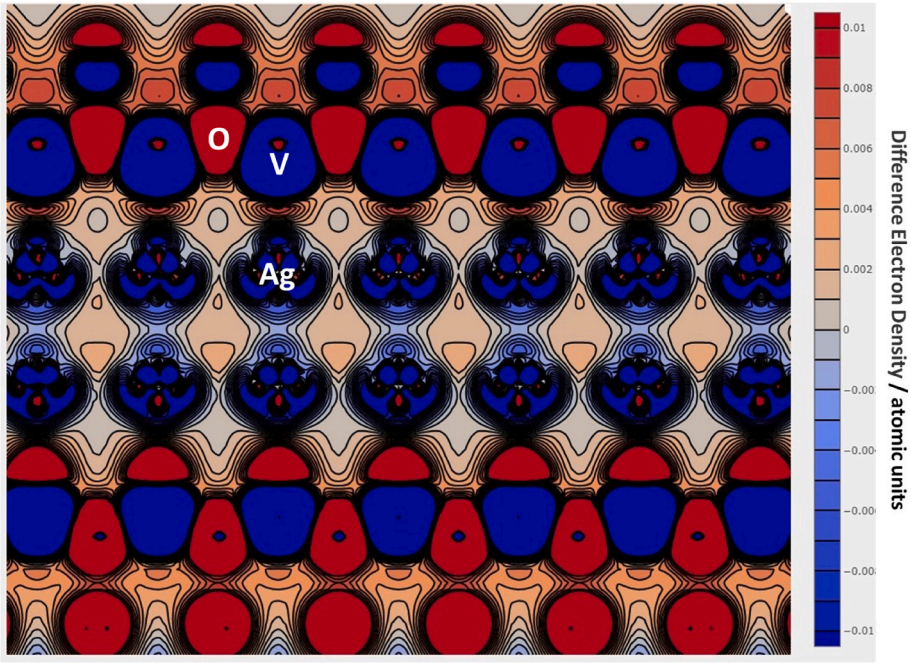

Fig. 8. – $AgVO_3$ charge density difference map.

heterostructure, and Raman spectroscopy suggested a plasmon effect associated with metallic Ag and β-$AgVO_3$ materials. Additionally, the work involves a detailed and systematic investigation of the theoretical β-$AgVO_3$ structure. It is observed that structural distortions and different atomic neighborhoods around a given atom may influence atomic charges presented in Ag_3VO_4 and β-$AgVO_3$ structures. Charge analysis indicated that the atomic charges in β-$AgVO_3$ differed from those in Ag_3VO_4, with Ag and V cations being more ionic in the $AgVO_3$ structure, while the largest atomic charge variation on O atoms indicated more and less ionic nature depending on of their atomic neighborhood for the β-$AgVO_3$ structure. It is also revealed unexpected chemical interactions in β-$AgVO_3$, including argentophilic and O–O interactions, which might contribute to understanding the growth of silver nanoparticles under electron irradiation. Understanding these chemical interactions and applying this method to produce the Ag_3VO_4/β-$AgVO_3$/Ag heterostructure may guide the manipulation of these materials to improve properties compared to traditional methods leading to greater performance in applications (catalysis, bactericidal activity, etc.). This study emphasizes the importance of both theoretical and experimental understanding of heterostructures for future technological advancements.

CRediT authorship contribution statement

Guilherme Henrique Cruvinel: Writing – review & editing, Writing – original draft, Visualization, Validation, Supervision, Project administration, Methodology, Investigation, Funding acquisition, Formal analysis, Data curation, Conceptualization. **Rafael de Queiroz Garcia:** Writing – review & editing, Visualization, Validation, Methodology. **Ivo Mateus Pinatti:** Writing – review & editing, Visualization, Validation. **Renan Augusto Pontes Ribeiro:** Writing – review & editing, Visualization, Validation, Methodology. **Leonardo De Boni:** Writing – review & editing, Visualization, Validation, Methodology. **Elson Longo:** Writing – review & editing, Writing – original draft, Visualization, Validation, Supervision, Project administration, Methodology, Investigation, Funding acquisition, Formal analysis, Data curation, Conceptualization.

Declaration of competing interest

The authors declare that they have no known competing financial interests or personal relationships that could have appeared to influence the work reported in this paper.

Acknowledgments

The authors are grateful for the financial support of São Paulo Research Foundation (FAPESP; Grant 2013/07296-2, 2018/03758-5, 2020/11232-3 and 2021/11255-6), and Coordenação de Aperfeiçoamento de Pessoal de Nível Superior-Brasil (CAPES) - Finance Code 001. We sincerely appreciate Professor Yvonne Primerano Mascarenhas from the Sao Carlos Institute of Physics (IFSC) of the University of Sao Paulo (USP) for generously providing both infrastructure and human resources from her laboratory to support the X-ray diffraction measurements.

Appendix A. Supplementary data

Supplementary data to this article can be found online at https://doi.org/10.1016/j.mtchem.2025.102738.

Data availability

Data will be made available on request.

References

[1] W.M. Steen, J. Mazumder, Laser Material Processing, fourth ed., Springer-Verlag, London, 2010.
[2] E. Assuncao, S. Williams, Comparison of continuous wave and pulsed wave laser welding effects, Opt. Lasers Eng. 51 (2013) 674–680, https://doi.org/10.1016/j.optlaseng.2013.01.007.
[3] M. Born, E. Wolf, Principles of Optics: Electromagnetic Theory of Propagation, Interference and Diffraction of Light, seventh ed., Cambridge University Press, 1999.
[4] L. Jiang, H.-L. Tsai, Energy transport and nanostructuring of dielectrics by femtosecond laser pulse trains, J. Heat Transf. 128 (2006) 926–933, https://doi.org/10.1115/1.2241979.
[5] R. Paschotta, Field Guide to Laser Pulse Generation, first ed., SPIE Press, Bellingham, 2008.

[6] S.C. Zilio, Óptica Moderna: Fundamentos e Aplicações, Universidade de São Paulo. Instituto de Física de São Carlos, 2016. www.livrosabertos.abcd.usp.br/portaldelivrosUSP/catalog/book/96. (Accessed 19 March 2024).
[7] C. Rulliere, Femtosecond Laser Pulses: Principles and Experiments, second ed., Springer, New York, 2004.
[8] M. Stafe, A. Marcu, N.N. Puscas, Pulsed Laser Ablation of Solids: Basics, Theory and Applications, first ed., Springer, 2014.
[9] M. Ams, D.J. Little, M.J. Withford, Femtosecond-laser-induced refractive index modifications for photonic device processing, in: N.A. Vainos (Ed.), Laser Growth Process. Photonic Devices, first ed., Woodhead Publishing, 2012, pp. 305–332, https://doi.org/10.1533/9780857096227.3.305.
[10] S.S. Mao, F. Quéré, S. Guizard, X. Mao, R.E. Russo, G. Petite, P. Martin, Dynamics of femtosecond laser interactions with dielectrics, Appl. Phys. A 79 (2004) 1695–1709, https://doi.org/10.1007/s00339-004-2684-0.
[11] L. Jiang, A.-D. Wang, B. Li, T.-H. Cui, Y.-F. Lu, Electrons dynamics control by shaping femtosecond laser pulses in micro/nanofabrication: modeling, method, measurement and application, Light Sci. Appl. 7 (2018), https://doi.org/10.1038/lsa.2017.134, 17134–17134.
[12] S.K. Sundaram, E. Mazur, Inducing and probing non-thermal transitions in semiconductors using femtosecond laser pulses, Nat. Mater. 1 (2002) 217–224, https://doi.org/10.1038/nmat767.
[13] C. Wang, L. Jiang, F. Wang, X. Li, Y.P. Yuan, H.L. Tsai, First-principles calculations of the electron dynamics during femtosecond laser pulse train material interactions, Phys. Lett. A 375 (2011) 3200–3204, https://doi.org/10.1016/j.physleta.2011.07.009.
[14] Y. Siegal, E.N. Glezer, E. Mazur, Dielectric constant of GaAs during a subpicosecond laser-induced phase transition, Phys. Rev. B 49 (1994) 16403–16406, https://doi.org/10.1103/PhysRevB.49.16403.
[15] Y. Siegal, E.N. Glezer, L. Huang, E. Mazur, Laser-induced phase transitions in semiconductors, Annu. Rev. Mater. Sci. 25 (1995) 223–247, https://doi.org/10.1146/annurev.ms.25.080195.001255.
[16] J.S. Graves, R.E. Allen, Response of GaAs to fast intense laser pulses, Phys. Rev. B 58 (1998) 13627–13633, https://doi.org/10.1103/PhysRevB.58.13627.
[17] P.L. Silvestrelli, A. Alavi, M. Parrinello, D. Frenkel, Ab initio molecular dynamics simulation of laser melting of silicon, Phys. Rev. Lett. 77 (1996) 3149–3152, https://doi.org/10.1103/PhysRevLett.77.3149.
[18] P. Stampfli, K.H. Bennemann, Theory for the laser-induced femtosecond phase transition of silicon and GaAS, Appl. Phys. A 60 (1995) 191–196, https://doi.org/10.1007/BF01538245.
[19] L. Cabral, E.R. Leite, E. Longo, M.A. San-Miguel, E.Z. da Silva, J. Andrés, Disentangling the effects of laser and electron irradiation on AgX (X = Cl, Br, and I): insights from quantum chemical calculations, Nano Lett. 24 (2024) 3021–3027, https://doi.org/10.1021/acs.nanolett.3c04130.
[20] W.D. Callister Jr., D.G. Rethwisch, Materials Science and Engineering: an Introduction, eighth ed., Wiley & Sons, New York, 2010.
[21] N.G. Macedo, T.R. Machado, R.A. Roca, M. Assis, C.C. Foggi, V. Puerto-Belda, G. Mínguez-Vega, A. Rodrigues, M.A. San-Miguel, E. Cordoncillo, H. Beltrán-Mir, J. Andrés, E. Longo, Tailoring the bactericidal activity of Ag nanoparticles/α-Ag2WO4 composite induced by electron beam and femtosecond laser irradiation: integration of experiment and computational modeling, ACS Appl. Bio Mater. 2 (2019) 824–837, https://doi.org/10.1021/acsabm.8b00673.
[22] R.C. Oliveira, C.C. Foggi, M.M. Teixeira, M.D.P. Silva, M. Assis, E.M. Francisco, B. N.A. da S. Pimentel, P.F. dos S. Pereira, C.E. Vergani, A.L. Machado, J. Andres, L. Gracia, E. Longo, Mechanism of antibacterial activity via morphology change of α-AgVO3: theoretical and experimental insights, ACS Appl. Mater. Interfaces 9 (2017) 11472–11481, https://doi.org/10.1021/acsami.7b00920.
[23] C.C. Foggi, R.C. Oliveira, M. Assis, M.T. Fabbro, V.R. Mastelaro, C.E. Vergani, L. Gracia, J. Andrés, E. Longo, A.L. Machado, Unveiling the role of β-Ag2MoO4 microcrystals to the improvement of antibacterial activity, Mater. Sci. Eng. C Mater. Biol. Appl. 111 (2020) 110765, https://doi.org/10.1016/j.msec.2020.110765.
[24] A. Vali, P.S. Toth, H.-W. Jee, F. Firouzan, C. Janáky, K.-J. Paeng, N. Myung, K. Rajeshwar, Electrosynthesis and properties of crystalline and phase-pure silver orthovanadate, J. Phys. Chem. C 124 (2020) 19980–19989, https://doi.org/10.1021/acs.jpcc.0c05421.
[25] S. Li, S. Hu, W. Jiang, Y. Liu, J. Liu, Z. Wang, Facile synthesis of flower-like Ag3VO4/Bi2WO6 heterojunction with enhanced visible-light photocatalytic activity, J. Colloid Interface Sci. 501 (2017) 156–163, https://doi.org/10.1016/j.jcis.2017.04.057.
[26] V. Cloet, A. Raw, K.R. Poeppelmeier, G. Trimarchi, H. Peng, J. Im, A.J. Freeman, N.H. Perry, T.O. Mason, A. Zakutayev, P.F. Ndione, D.S. Ginley, J.D. Perkins, Structural, optical, and transport properties of α- and β-Ag3VO4, Chem. Mater. 24 (2012) 3346–3354, https://doi.org/10.1021/cm301119c.
[27] T.A. Albrecht, C.L. Stern, K.R. Poeppelmeier, The Ag2O-V2O5-HF((Aq)) system and crystal structure of alpha-Ag3VO4, Inorg. Chem. 46 (2007) 1704–1708, https://doi.org/10.1021/ic062138+.
[28] G. Trimarchi, H. Peng, J. Im, A.J. Freeman, V. Cloet, A. Raw, K.R. Poeppelmeier, K. Biswas, S. Lany, A. Zunger, Using design principles to systematically plan the synthesis of hole-conducting transparent oxides: Cu3VO4 and Ag3VO4 as a case study, Phys. Rev. B 84 (2011) 165116, https://doi.org/10.1103/PhysRevB.84.165116.
[29] C. Belver, C. Adán, S. García-Rodríguez, M. Fernández-García, Photocatalytic behavior of silver vanadates: microemulsion synthesis and post-reaction characterization, Chem. Eng. J. 224 (2013) 24–31, https://doi.org/10.1016/j.cej.2012.11.102.
[30] W.D. Chemelewski, O. Mabayoje, C.B. Mullins, SILAR growth of Ag3VO4 and characterization for photoelectrochemical water oxidation, J. Phys. Chem. C 119 (2015) 26803–26808, https://doi.org/10.1021/acs.jpcc.5b06658.
[31] L. Zhang, Y. He, P. Ye, W. Qin, Y. Wu, T. Wu, Enhanced photodegradation activity of rhodamine B by Co3O4/Ag3VO4 under visible light irriadiation, Mater. Sci. Eng. B 178 (2013) 45–52, https://doi.org/10.1016/j.mseb.2012.10.011.
[32] P. Raizada, A. Aslam Parwaz Khan, P. Singh, Construction of carbon nanotube mediated Fe doped graphitic carbon nitride and Ag3VO4 based Z-scheme heterojunction for H2O2 assisted 2,4 dimethyl phenol photodegradation, Sep. Purif. Technol. 247 (2020) 116957, https://doi.org/10.1016/j.seppur.2020.116957.
[33] P. Raizada, A. Sudhaik, P. Singh, P. Shandilya, A.K. Saini, V.K. Gupta, J.-H. Lim, H. Jung, A. Hosseini-Bandegharaei, Fabrication of Ag3VO4 decorated phosphorus and sulphur Co-doped graphitic carbon nitride as a high-dispersed photocatalyst for phenol mineralization and E. Coli disinfection, Sep. Purif. Technol. 212 (2019) 887–900, https://doi.org/10.1016/j.seppur.2018.12.007.
[34] L. Gao, Z. Li, J. Liu, Facile synthesis of Ag3VO4/β-AgVO3 nanowires with efficient visible-light photocatalytic activity, RSC Adv. 7 (2017) 27515–27521, https://doi.org/10.1039/C7RA03955G.
[35] X. Lv, J. Wang, Z. Yan, D. Jiang, J. Liu, Design of 3D H-BN architecture as Ag3VO4 enhanced photocatalysis stabilizer and promoter, J. Mol. Catal. Chem. 418–419 (2016) 146–153, https://doi.org/10.1016/j.molcata.2016.03.036.
[36] X. Hu, C. Hu, Preparation and visible-light photocatalytic activity of Ag3VO4 powders, J. Solid State Chem. 180 (2007) 725–732, https://doi.org/10.1016/j.jssc.2006.11.032.
[37] X. Yan, X. Yuan, J. Wang, Q. Wang, C. Zhou, D. Wang, H. Tang, J. Pan, X. Cheng, Construction of novel ternary dual Z-scheme Ag3VO4/C3N4/reduced TiO2 composite with excellent visible-light photodegradation activity, J. Mater. Res. 34 (2019) 2024–2036, https://doi.org/10.1557/jmr.2019.164.
[38] V.R. Raja, D.R. Rosaline, A. Suganthi, M. Rajarajan, Ultrasonic assisted synthesis with enhanced visible-light photocatalytic activity of NiO/Ag3VO4 nanocomposite and its antibacterial activity, Ultrason. Sonochem. 44 (2018) 73–85, https://doi.org/10.1016/j.ultsonch.2018.02.010.
[39] F. Kiantazh, A. Habibi-Yangjeh, Ag3VO4/ZnO nanocomposites with an n– n heterojunction as novel visible-light-driven photocatalysts with highly enhanced activity, Mater. Sci. Semicond. Process. 39 (2015) 671–679, https://doi.org/10.1016/j.mssp.2015.06.011.
[40] D.P. Sahoo, S. Patnaik, D. Rath, K.M. Parida, Synergistic effects of plasmon induced Ag@Ag3VO4/ZnCr LDH ternary heterostructures towards visible light responsive O2 evolution and phenol oxidation reactions, Inorg. Chem. Front. 5 (2018) 879–896, https://doi.org/10.1039/C7QI00742F.
[41] G.H. Cruvinel, R.C. de Oliveira, M.C. de Oliveira, I.M. Pinatti, R.A.P. Ribeiro, E. Longo, Unraveling the morphology-structure-property relationship of silver orthovanadate p-semiconductor: experimental and theoretical investigation, Ceram. Int. 50 (2024) 29568–29579, https://doi.org/10.1016/j.ceramint.2024.05.252.
[42] R.E. Dinnebier, A. Kowalevsky, H. Reichert, M. Jansen, Polymorphism of Ag3VO4, Z. Für Krist 222 (2007) 420–426, https://doi.org/10.1524/zkri.2007.222.8.420.
[43] P. Rozier, J.-M. Savariault, J. Galy, β AgVO3 crystal structure and relationships with Ag2V4O11and δ AgxV2O5, J. Solid State Chem. 122 (1996) 303–308, https://doi.org/10.1006/jssc.1996.0117.
[44] Y. Chen, Y. Wei, P. Chang, L. Ye, Morphology-controlled synthesis of monodisperse silver spheres via a solvothermal method, J. Alloys Compd. 509 (2011) 5381–5387, https://doi.org/10.1016/j.jallcom.2011.02.054.
[45] A.D. Becke, Density-functional exchange-energy approximation with correct asymptotic behavior, Phys. Rev. A 38 (1988) 3098–3100, https://doi.org/10.1103/PhysRevA.38.3098.
[46] C. Lee, W. Yang, R.G. Parr, Development of the colle-salvetti correlation-energy formula into a functional of the electron density, Phys. Rev. B Condens. Matter 37 (1988) 785–789, https://doi.org/10.1103/physrevb.37.785.
[47] S. Grimme, J. Antony, S. Ehrlich, H. Krieg, A consistent and accurate ab initio parametrization of density functional dispersion correction (DFT-D) for the 94 elements H-Pu, J. Chem. Phys. 132 (2010) 154104, https://doi.org/10.1063/1.3382344.
[48] R. Dovesi, A. Erba, R. Orlando, C.M. Zicovich-Wilson, B. Civalleri, L. Maschio, M. Rérat, S. Casassa, J. Baima, S. Salustro, B. Kirtman, Quantum-mechanical condensed matter simulations with CRYSTAL, WIREs Comput. Mol. Sci. 8 (2018) e1360, https://doi.org/10.1002/wcms.1360.
[49] T. Bredow, K. Jug, R.A. Evarestov, Electronic and magnetic structure of ScMnO3, Phys. Status Solidi B 243 (2006) R10–R12, https://doi.org/10.1002/pssb.200541403.
[50] E. Aprà, E. Stefanovich, R. Dovesi, C. Roetti, An ab initio hartree—fock study of silver chloride, Chem. Phys. Lett. 186 (1991) 329–335, https://doi.org/10.1016/0009-2614(91)90187-E.
[51] W.C. Mackrodt, N.M. Harrison, V.R. Saunders, N.L. Allan, M.D. Towler, E. Aprà, R. Dovesi, Ab initio Hartree-Fock calculations of CaO, VO, MnO and NiO, Philos. Mag. A 68 (1993) 653–666, https://doi.org/10.1080/01418619308213989.
[52] H.J. Monkhorst, J.D. Pack, Special points for brillouin-zone integrations, Phys. Rev. B 13 (1976) 5188–5192, https://doi.org/10.1103/PhysRevB.13.5188.
[53] L. Maschio, B. Kirtman, M. Rérat, R. Orlando, R. Dovesi, Ab initio analytical Raman intensities for periodic systems through a coupled perturbed Hartree-Fock/Kohn-Sham method in an atomic orbital basis. II. Validation and comparison with experiments, J. Chem. Phys. 139 (2013) 164102, https://doi.org/10.1063/1.4824443.

[54] F. Pascale, C.M. Zicovich-Wilson, F. López Gejo, B. Civalleri, R. Orlando, R. Dovesi, The calculation of the vibrational frequencies of crystalline compounds and its implementation in the CRYSTAL code, J. Comput. Chem. 25 (2004) 888–897, https://doi.org/10.1002/jcc.20019.

[55] C.M. Zicovich-Wilson, F. Pascale, C. Roetti, V.R. Saunders, R. Orlando, R. Dovesi, Calculation of the vibration frequencies of alpha-quartz: the effect of Hamiltonian and basis set, J. Comput. Chem. 25 (2004) 1873–1881, https://doi.org/10.1002/jcc.20120.

[56] C. Gatti, S. Casassa, TOPOND14 user's manual, CNR-ISTM of milano, milano. https://www.crystal.unito.it/topond/topond.pdf, 2017. (Accessed 14 December 2023).

[57] R.F.W. Bader, Atoms in Molecules: A Quantum Theory, Oxford University Press, Oxford, 1990.

[58] C.F. Holder, R.E. Schaak, Tutorial on powder X-ray diffraction for characterizing nanoscale materials, ACS Nano 13 (2019) 7359–7365, https://doi.org/10.1021/acsnano.9b05157.

[59] A.D. Prasetya, M. Rifai, Mujamilah, H. Miyamoto, X-ray diffraction (XRD) profile analysis of pure ECAP-annealing Nickel samples, J. Phys. Conf. Ser. 1436 (2020) 012113, https://doi.org/10.1088/1742-6596/1436/1/012113.

[60] M. Assis, T. Robeldo, C.C. Foggi, A.M. Kubo, G. Mínguez-Vega, E. Condoncillo, H. Beltran-Mir, R. Torres-Mendieta, J. Andrés, M. Oliva, C.E. Vergani, P. A. Barbugli, E.R. Camargo, R.C. Borra, E. Longo, Ag nanoparticles/α-Ag 2 WO 4 composite formed by electron beam and femtosecond irradiation as potent antifungal and antitumor agents, Sci. Rep. 9 (2019) 9927, https://doi.org/10.1038/s41598-019-46159-y.

[61] Y. Miyasaka, M. Hashida, T. Nishii, S. Inoue, S. Sakabe, Derivation of effective penetration depth of femtosecond laser pulses in metal from ablation rate dependence on laser fluence, incidence angle, and polarization, Appl. Phys. Lett. 106 (2015) 013101, https://doi.org/10.1063/1.4905353.

[62] D. Bäuerle, Laser Processing and Chemistry, fourth ed., Springer, Heidelberg, 2011.

[63] B.C. Stuart, M.D. Feit, A.M. Rubenchik, B.W. Shore, M.D. Perry, Laser-induced damage in dielectrics with nanosecond to subpicosecond pulses, Phys. Rev. Lett. 74 (1995) 2248–2251, https://doi.org/10.1103/PhysRevLett.74.2248.

[64] B.C. Stuart, M.D. Feit, S. Herman, A.M. Rubenchik, B.W. Shore, M.D. Perry, Nanosecond-to-femtosecond laser-induced breakdown in dielectrics, Phys. Rev. B 53 (1996) 1749–1761, https://doi.org/10.1103/PhysRevB.53.1749.

[65] R.C. Oliveira, M. Assis, M.M. Teixeira, M.D.P. Silva, M.S. Li, J. Andres, L. Gracia, E. Longo, An experimental and computational study of β-AgVO3: optical properties and formation of Ag nanoparticles, J. Phys. Chem. C 120 (2016) 12254–12264, https://doi.org/10.1021/acs.jpcc.6b02840.

[66] A. Beltrán, L. Gracia, J. Andrés, E. Longo, First-principles study on polymorphs of AgVO3: assessing to structural stabilities and pressure-induced transitions, J. Phys. Chem. C 121 (2017) 27624–27642, https://doi.org/10.1021/acs.jpcc.7b09865.

[67] P. Saeta, J.-K. Wang, Y. Siegal, N. Bloembergen, E. Mazur, Ultrafast electronic disordering during femtosecond laser melting of GaAs, Phys. Rev. Lett. 67 (1991) 1023–1026, https://doi.org/10.1103/PhysRevLett.67.1023.

[68] J.P. Callan, A.M.-T. Kim, L. Huang, E. Mazur, Ultrafast electron and lattice dynamics in semiconductors at high excited carrier densities, Chem. Phys. 251 (2000) 167–179, https://doi.org/10.1016/S0301-0104(99)00301-8.

[69] J.P. Callan, A.M.-T. Kim, C.A.D. Roeser, E. Mazur, Universal dynamics during and after ultrafast laser-induced semiconductor-to-metal transitions, Phys. Rev. B 64 (2001) 073201, https://doi.org/10.1103/PhysRevB.64.073201.

[70] E.N. Glezer, Y. Siegal, L. Huang, E. Mazur, Laser-induced band-gap collapse in GaAs, Phys. Rev. B 51 (1995) 6959–6970, https://doi.org/10.1103/PhysRevB.51.6959.

[71] L. Huang, J.P. Callan, E.N. Glezer, E. Mazur, GaAs under intense ultrafast excitation: response of the dielectric function, Phys. Rev. Lett. 80 (1998) 185–188, https://doi.org/10.1103/PhysRevLett.80.185.

[72] X. Kong, Z. Guo, C. Zeng, J. Huang, L. Cao, L. Li, L. Yin, P. Wen, Q. Feng, Z. Xu, Soft chemical in situ synthesis, formation mechanism and electrochemical performances of 1D bead-like AgVO3 nanoarchitectures, J. Mater. Chem. A 3 (2015) 18127–18135, https://doi.org/10.1039/C5TA05110J.

[73] S.-J. Bao, Q.-L. Bao, C.-M. Li, T.P. Chen, C.-Q. Sun, Z.-L. Dong, Y. Gan, J. Zhang, Synthesis and electrical transport of novel channel-structured beta-AgVO3, Small Weinh. Bergstr. Ger. 3 (2007) 1174–1177, https://doi.org/10.1002/smll.200700032.

[74] J.-M. Song, Y.-Z. Lin, H.-B. Yao, F.-J. Fan, X.-G. Li, S.-H. Yu, Superlong β-AgVO3 nanoribbons: high-yield synthesis by a pyridine-assisted solution approach, their stability, electrical and electrochemical properties, ACS Nano 3 (2009) 653–660, https://doi.org/10.1021/nn800813s.

[75] W. Zhao, Y. Guo, S. Wang, H. He, C. Sun, S. Yang, A novel ternary plasmonic photocatalyst: ultrathin g-C3N4 nanosheet hybrided by Ag/AgVO3 nanoribbons with enhanced visible-light photocatalytic performance, Appl. Catal. B Environ. 165 (2015) 335–343, https://doi.org/10.1016/j.apcatb.2014.10.016.

[76] R.D. Holtz, B.A. Lima, A.G. Souza Filho, M. Brocchi, O.L. Alves, Nanostructured silver vanadate as a promising antibacterial additive to water-based paints, Nanomedicine Nanotechnol. Biol. Med. 8 (2012) 935–940, https://doi.org/10.1016/j.nano.2011.11.012.

[77] R.L. Frost, K.L. Erickson, M.L. Weier, O. Carmody, Raman and infrared spectroscopy of selected vanadates, Spectrochim. Acta. A. Mol. Biomol. Spectrosc. 61 (2005) 829–834, https://doi.org/10.1016/j.saa.2004.06.006.

[78] P. Vandenabeele, Practical Raman Spectroscopy: an Introduction, John Wiley & Sons, Chichester, 2013.

[79] E. Smith, G. Dent, Modern Raman Spectroscopy: A Practical Approach, first ed., John Wiley & Sons, Chichester, 2005.

[80] Z. Zalevsky, I. Abdulhalim, Integrated Nanophotonic Devices, second ed., William Andrew, 2014.

[81] M. Assis, E. Cordoncillo, R. Torres-Mendieta, H. Beltrán-Mir, G. Mínguez-Vega, R. Oliveira, E.R. Leite, C.C. Foggi, C.E. Vergani, E. Longo, J. Andrés, Towards the scale-up of the formation of nanoparticles on α-Ag 2 WO 4 with bactericidal properties by femtosecond laser irradiation, Sci. Rep. 8 (2018) 1884, https://doi.org/10.1038/s41598-018-19270-9.

[82] C.C. dos Santos, M. Assis, T.R. Machado, P.F. dos S. Pereira, G. Minguez-Vega, E. Cordoncillo, H. Beltran-Mir, C. Doñate-Buendía, J. Andrés, E. Longo, Proof-of-Concept studies directed toward the formation of metallic Ag nanostructures from Ag $_3$ PO $_4$ induced by electron beam and femtosecond laser, Part. Part. Syst. Charact. 36 (2019) 1800533, https://doi.org/10.1002/ppsc.201800533.

[83] J.C. Souza, R.A.P. Ribeiro, L.G. da Trindade, R.C. de Oliveira, L.D. Costa, M.C. de Oliveira, S.R. de Lazaro, J.R. Sambrano, C.R. Mendonça, L. de Boni, F.M. L. Pontes, A.J.A. de Oliveira, E.R. Leite, E. Longo, Unconventional disorder by femtosecond laser irradiation in Fe2O3, ACS Omega 6 (2021) 28049–28062, https://doi.org/10.1021/acsomega.1c04079.

[84] I.M. Pinatti, A.F. Gouveia, C. Doñate-Buendía, G. Mínguez-Vega, J. Andrés, E. Longo, Femtosecond-laser-irradiation-induced structural organization and crystallinity of Bi2WO6, Sci. Rep. 10 (2020) 4613, https://doi.org/10.1038/s41598-020-61524-y.

[85] T. Váczi, A new, simple approximation for the deconvolution of instrumental broadening in spectroscopic band profiles, Appl. Spectrosc. 68 (2014) 1274–1278, https://doi.org/10.1366/13-07275.

[86] J. Thyr, T. Edvinsson, Evading the illusions: identification of false peaks in micro-Raman spectroscopy and guidelines for scientific best practice, Angew. Chem. Int. Ed. 62 (2023) e202219047, https://doi.org/10.1002/anie.202219047.

[87] H.-C. Huang, J.I. Dadap, I.P. Herman, H. Bakhru, R.M. Osgood, Micro-Raman spectroscopic visualization of lattice vibrations and strain in He^{+}- implanted single-crystal $LiNbO_3$, Opt. Mater. Express 4 (2014) 338–345, https://doi.org/10.1364/OME.4.000338.

[88] S. Mignuzzi, A.J. Pollard, N. Bonini, B. Brennan, I.S. Gilmore, M.A. Pimenta, D. Richards, D. Roy, Effect of disorder on Raman scattering of single-layer MoS2, Phys. Rev. B 91 (2015) 195411, https://doi.org/10.1103/PhysRevB.91.195411.

[89] M. Kitajima, Defects in crystals studied by Raman scattering, Crit. Rev. Solid State Mater. Sci. 22 (1997) 275–349, https://doi.org/10.1080/10408439708241263.

[90] C.M. Ruiz, X. Fontané, A. Fairbrother, V. Izquierdo-Roca, C. Broussillou, S. Bodnar, A. Pérez-Rodríguez, V. Bermúdez, Impact of electronic defects on the Raman spectra from electrodeposited Cu(In,Ga)Se2 solar cells: application for non-destructive defect assessment, Appl. Phys. Lett. 102 (2013) 091106, https://doi.org/10.1063/1.4793418.

[91] D.E. Newbury, N.W.M. Ritchie, Is scanning electron microscopy/energy dispersive X-ray spectrometry (SEM/EDS) quantitative? Scanning 35 (2013) 141–168, https://doi.org/10.1002/sca.21041.

[92] D.A. Wollman, K.D. Irwin, G.C. Hilton, L.L. Dulcie, D.E. Newbury, J.M. Martinis, High-resolution, energy-dispersive microcalorimeter spectrometer for X-ray microanalysis, J. Microsc. 188 (1997) 196–223, https://doi.org/10.1046/j.1365-2818.1997.2670824.x.

[93] S. Chandramohan, A. Kanjilal, J.K. Tripathi, S.N. Sarangi, R. Sathyamoorthy, T. Som, Structural and optical properties of Mn-doped CdS thin films prepared by ion implantation, J. Appl. Phys. 105 (2009) 123507, https://doi.org/10.1063/1.3151712.

[94] S.B. Aziz, S.M. Mamand, S.R. Saed, R.M. Abdullah, S.A. Hussein, New method for the development of plasmonic metal-semiconductor interface layer: polymer composites with reduced energy band gap, J. Nanomater. 2017 (2017) e8140693, https://doi.org/10.1155/2017/8140693.

[95] T. Tan, C. Tian, Z. Ren, J. Yang, Y. Chen, L. Sun, Z. Li, A. Wu, J. Yin, H. Fu, LSPR-dependent SERS performance of silver nanoplates with highly stable and broad tunable LSPRs prepared through an improved seed-mediated strategy, Phys. Chem. Chem. Phys. 15 (2013) 21034–21042, https://doi.org/10.1039/C3CP52236A.

[96] R.-A. Eichel, Defect structure of oxide ferroelectrics—valence state, site of incorporation, mechanisms of charge compensation and internal bias fields, J. Electroceramics 19 (2007) 11–23, https://doi.org/10.1007/s10832-007-9068-8.

[97] R.-A. Eichel, Structural and dynamic properties of oxygen vacancies in perovskite oxides—analysis of defect chemistry by modern multi-frequency and pulsed EPR techniques, Phys. Chem. Chem. Phys. 13 (2010) 368–384, https://doi.org/10.1039/B918782K.

[98] L. Zhang, H. Hao, S. Zhang, M.T. Lanagan, Z. Yao, Q. Xu, J. Xie, J. Zhou, M. Cao, H. Liu, Defect structure-electrical property relationship in Mn-doped calcium strontium titanate dielectric ceramics, J. Am. Ceram. Soc. 100 (2017) 4638–4648, https://doi.org/10.1111/jace.14994.

[99] S. Upadhyay, J. Shrivastava, A. Solanki, S. Choudhary, V. Sharma, P. Kumar, N. Singh, V.R. Satsangi, R. Shrivastav, U.V. Waghmare, S. Dass, Enhanced photoelectrochemical response of BaTiO3 with Fe doping: experiments and first-principles analysis, J. Phys. Chem. C 115 (2011) 24373–24380, https://doi.org/10.1021/jp202863a.

[100] M.S. Alkathy, M.H. Lente, J.A. Eiras, Bandgap narrowing of Ba0.92Na0.04Bi0.04TiO3 ferroelectric ceramics by transition metals doping for photovoltaic applications, Mater. Chem. Phys. 257 (2021) 123791, https://doi.org/10.1016/j.matchemphys.2020.123791.

[101] J. Hui, G. Zhang, C. Ni, J.T.S. Irvine, Promoting photocatalytic H2 evolution by tuning cation deficiency in La and Cr co-doped SrTiO3, Chem. Commun. 53 (2017) 10038–10041, https://doi.org/10.1039/C7CC05144A.
[102] A. Sagdeo, A. Nagwanshi, P. Pokhriyal, A.K. Sinha, P. Rajput, V. Mishra, P. R. Sagdeo, Disappearance of dielectric anomaly in spite of presence of structural phase transition in reduced BaTiO3: effect of defect states within the bandgap, J. Appl. Phys. 123 (2018) 161424, https://doi.org/10.1063/1.5010870.
[103] M.S. Alkathy, F.L. Zabotto, K.C.J. Raju, J.A. Eiras, Effect of defects on the band gap and photoluminescence emission of Bi and Li co-substituted barium strontium titanate ceramics, Mater. Chem. Phys. 275 (2022) 125235, https://doi.org/10.1016/j.matchemphys.2021.125235.
[104] A.E. Mesoudy, D. Machon, A. Ruediger, A. Jaouad, F. Alibart, S. Ecoffey, D. Drouin, Band gap narrowing induced by oxygen vacancies in reactively sputtered TiO2 thin films, Thin Solid Films 769 (2023) 139737, https://doi.org/10.1016/j.tsf.2023.139737.
[105] B.R.C. Menezes, R.G. Ribas, V.M. Schatkoski, T.L. do Amaral Montanheiro, C. Y. Koga-Ito, G.P. Thim, Synthesis of β-AgVO3 nanowires by hydrothermal and precipitation routes: a comparative study, SN Appl. Sci. 1 (2019) 1327, https://doi.org/10.1007/s42452-019-1396-1.
[106] E. Espinosa, I. Alkorta, J. Elguero, E. Molins, From weak to strong interactions: a comprehensive analysis of the topological and energetic properties of the electron density distribution involving X–H···F–Y systems, J. Chem. Phys. 117 (2002) 5529–5542, https://doi.org/10.1063/1.1501133.
[107] C. Gatti, Chemical bonding in crystals: new directions, Z. Für Krist. - Cryst. Mater. 220 (2005) 399–457, https://doi.org/10.1524/zkri.220.5.399.65073.
[108] M.V. Vener, A.V. Manaev, A.N. Egorova, V.G. Tsirelson, QTAIM study of strong H-bonds with the O-H…a fragment (A=O, N) in three-dimensional periodical crystals, J. Phys. Chem. A 111 (2007) 1155–1162, https://doi.org/10.1021/jp067057d.
[109] D.V. Korabel'nikov, Y.N. Zhuravlev, The nature of the chemical bond in oxyanionic crystals based on QTAIM topological analysis of electron densities, RSC Adv. 9 (2019) 12020–12033, https://doi.org/10.1039/C9RA01403A.
[110] P. Rozier, J.-M. Savariault, J. Galy, β AgVO3 crystal structure and relationships with Ag2V4O11 and δ AgxV2O5, J. Solid State Chem. 122 (1996) 303–308, https://doi.org/10.1006/jssc.1996.0117.
[111] V. Tsirelson, Y. Abramov, V. Zavodnik, A. Stash, E. Belokoneva, J. Stahn, U. Pietsch, D. Feil, Critical points in a crystal and procrystal, Struct. Chem. 9 (1998) 249–254, https://doi.org/10.1023/A:1022474712532.
[112] S.J. Grabowski, What is the covalency of hydrogen bonding? Chem. Rev. 111 (2011) 2597–2625, https://doi.org/10.1021/cr800346f.
[113] Y. Kuwayama, K. Hirose, N. Sata, Y. Ohishi, The pyrite-type high-pressure form of silica, Science 309 (2005) 923–925, https://doi.org/10.1126/science.1114879.
[114] G.V. Gibbs, M.A. Spackman, D. Jayatilaka, K.M. Rosso, D.F. Cox, Bond length and local energy density property connections for non-transition-metal oxide-bonded interactions, J. Phys. Chem. A 110 (2006) 12259–12266, https://doi.org/10.1021/jp062992m.
[115] Y.V. Nelyubina, M.Y. Antipin, K.A. Lyssenko, Anion–anion interactions: their nature, energy and role in crystal formation, Russ. Chem. Rev. 79 (2010) 167, https://doi.org/10.1070/RC2010v079n03ABEH004120.